J. Fluid Mech. (2023), *vol.* 975, A29, doi:10.1017/jfm.2023.869

JFM PAPERS

Experimental study on Richtmyer–Meshkov instability at a light–heavy interface over a wide range of Atwood numbers

Chenren Chen[1], **Yinuo Xing**[1], **He Wang**[1,†], **Zhigang Zhai**[1] and **Xisheng Luo**[1,2,†]

[1]Advanced Propulsion Laboratory, Department of Modern Mechanics, University of Science and Technology of China, Hefei 230026, PR China

[2]State Key Laboratory of High Temperature Gas Dynamics, Institute of Mechanics, Chinese Academy of Sciences, Beijing 100190, PR China

(Received 24 May 2023; revised 16 September 2023; accepted 13 October 2023)

Richtmyer–Meshkov instability (RMI) at a light–heavy single-mode interface over a wide range of post-shock Atwood numbers A_1 is studied systematically through elaborate experiments. The interface generation and A_1 variation are achieved by the soap-film technology and gas-layer scheme, respectively. Qualitatively, the nonlinear interface evolution features, including spike, bubble and roll-up structures, are more significant in RMI with higher A_1. Quantitatively, both the impulsive model and an analytical linear model perform well in predicting the linear growth rate under a wide range of A_1 conditions. For the weakly nonlinear stage, the significant spike acceleration occurring when A_1 is high, which is observed experimentally for the first time, results in the evolution law of RMI with high A_1 being different from the counterpart with low or intermediate A_1. None of the considered nonlinear models is found to be applicable for RMI under all A_1 conditions, and the predictive capabilities of these models are analysed and summarized. Based on the present experimental results, an empirical nonlinear model is proposed for RMI over a wide range of A_1. Further, modal analysis shows that in RMI with high (low or intermediate) A_1, high-order harmonics evolve rapidly (slowly) and cannot (can) be ignored. Accordingly, for RMI with high (low or intermediate) A_1, the modal model proposed by Zhang & Sohn (*Phys. Fluids*, vol. 9, 1997, pp. 1106–1124) is less (more) accurate than the one proposed by Vandenboomgaerde *et al.* (*Phys. Fluids*, vol. 14, 2002, pp. 1111–1122), since the former ignores perturbation solutions higher than fourth order (the latter retains only terms with the highest power in time).

Key words: shock waves

† Email addresses for correspondence: ustchewang@ustc.edu.cn, xsluo@imech.ac.cn

1. Introduction

Richtmyer–Meshkov instability (RMI) (Richtmyer 1960; Meshkov 1969) occurs when a perturbed interface separating two substances of different densities is accelerated by a shock wave. It has gained extensive attention for decades due to its crucial role in many important scientific and engineering fields, such as inertial confinement fusion (ICF) (Nuckolls *et al.* 1972; Lindl *et al.* 2014; Betti & Hurricane 2016), supernova explosion (Arnett *et al.* 1989; Kuranz *et al.* 2018), scramjet (Billig 1993; Yang, Kubota & Zukoski 1993), shock-flame interaction (Khokhlov *et al.* 1999*a*; Khokhlov, Oran & Thomas 1999*b*), and so on. Comprehensive insights and specific details regarding RMI and its applications can be found in several recent systematic reviews (Zhou 2017*a*,*b*; Zhou *et al.* 2019, 2021). For ICF, RMI is one of the tremendous obstacles to its realization, and the effect of RMI is highly related to the target design (Kritcher *et al.* 2022). There are several types of target in ICF, such as the typical target with one ablative layer made of one main material, and the innovative target with multiple ablative layers formed of different main materials (Lindl 1995; Qiao & Lan 2021; Kritcher *et al.* 2022). In addition, the main materials for the ablative layer are diverse, including CH plastic and high-density carbon, etc. (Lindl *et al.* 2014). In other words, the Atwood number (defined as $A = (\rho_j - \rho_i)/(\rho_j + \rho_i)$, with ρ_i and ρ_j being the densities of substances upstream and downstream of the interface, respectively) of the interface separating deuterium-tritium ice and ablator or different ablative layers can be significantly different for different targets. Therefore, it is necessary and desirable to study the evolution of RMI under various A conditions. Pre- and post-shock A (A_0 and A_1) are equivalent in incompressible RMI, but inequivalent in compressible RMI. Since we consider the compressible RMI in this work, A generally refers specifically to A_1 containing information on the compressibility of the flow field.

For RMI with small scaled initial amplitude ka_0 (where k and a_0 are perturbation wavenumber and initial amplitude, respectively), the perturbation amplitude a first varies at an increasing rate due to the start-up process (Richtmyer 1960; Lombardini & Pullin 2009), and then enters a linear growth period until nonlinearity becomes pronounced. Theoretically, Richtmyer (1960) first investigated RMI on a light–heavy interface and deduced a compressible linear theory for forecasting the amplitude growth rate $\dot{a}$ in the linear regime. On the basis of the compressible linear theory, a semi-empirical model, i.e. the impulsive model, was proposed for predicting the linear asymptotic amplitude growth rate $\dot{a}_1$. Notably, the impulsive model loses accuracy with the increase of the flow compressibility (Mikaelian 1994; Yang, Zhang & Sharp 1994). An exact compressible linear theory that, in principle, is capable of solving for $\dot{a}$ within the linear regime under arbitrary flow compressibility conditions was deduced by Wouchuk & Nishihara (1996). Based on the compressible linear theory, Wouchuk & Nishihara (1997) proposed an analytical solution (the WN model) to predict $\dot{a}_1$, and obtained a simplified model in the weak shock limit (the WN-WL model). Subsequently, the WN model was modified further by Wouchuk (2001). RMI was first studied experimentally by Meshkov (1969) using interfaces formed by nitrocellulose membranes. Different gas combinations on both sides of the interface were considered to achieve a wide variation of A_1. It was found that the experimental $\dot{a}_1$ (denoted $\dot{a}_1^e$) is qualitatively consistent with the impulsive model prediction (denoted $\dot{a}_1^i$): both are positively related to A_1. However, quantitatively, all $\dot{a}_1^e$ are significantly lower than the corresponding $\dot{a}_1^i$, possibly due to the effects of high amplitude and membrane. Jones & Jacobs (1997) investigated experimentally the shock-induced evolution of a continuous N_2–SF_6 interface with $A_0 = 0.67$. Although the agreement between $\dot{a}_1^e$ and $\dot{a}_1^i$ is better relative to that in previous work

(Meshkov 1969), $\dot{a}_1^e$ is still lower than $\dot{a}_1^i$ due to the diffusion layer. By dropping a two-liquid system mounted on a sled onto a coil spring to produce a nearly impulsive upward acceleration, Niederhaus & Jacobs (2003) studied experimentally incompressible RMI with low negative A_1 ($= -0.1587$). Very clear views of the developing interface were realized using planar laser-induced fluorescence imaging. Due to the extended duration of the acceleration pulse, the theoretical $\dot{a}_1$ was determined by integrating numerically the first-order time derivative of the impulsive model. A remarkably good agreement between the theoretical and experimental results was reached for a dimensionless time up to 0.3. Using the soap-film technique to generate an interface free of solid membrane and diffusion layer, Liu *et al.* (2018) studied elaborately the evolution of a shocked air–SF_6 single-mode interface, and provided the first direct experimental validation of the impulsive model. However, A_1 in the work of Liu *et al.* (2018) is within a narrow range ($0.54 \leq A_1 \leq 0.61$), and it is desirable to examine the impulsive model over a wider range of A_1.

In the early stages of RMI, since the perturbed waves are close to interface and ka is small, compressibility dominates the perturbation evolution while nonlinearity is less important. As perturbed waves move away from the interface and ka increases, compressibility becomes weaker and nonlinearity begins to dominate the perturbation growth (Zhang & Sohn 1997). In other words, RMI has different dominant mechanisms at different evolution stages, making its overall evolution behaviour from linear to nonlinear stages difficult to describe rigorously. Fortunately, RMI can be approximated as a linear compressible physical process in the early stages and as a nonlinear incompressible one in the late stages (Zhang & Sohn 1997). Referring to this idea, several empirical nonlinear models were proposed (Zhang & Sohn 1997; Sadot *et al.* 1998; Mikaelian 2003; Dimonte & Ramaprabhu 2010; Zhang & Guo 2016, 2022), and they are briefly reviewed as follows.

Zhang & Sohn (1997) first derived the perturbation series of the amplitude growth rates of spike, bubble and entire interface ($\dot{a}_s$, $\dot{a}_b$ and $\dot{a}$). Then, by applying the Padé approximation to extend the valid range of the perturbation series, an approximate nonlinear solution was derived. Finally, through matching the linear and nonlinear solutions, a nonlinear model known as the ZS model was obtained. Sadot *et al.* (1998) proposed a nonlinear model (the SEA model) by matching the impulsive model prediction, perturbation expansion solution and potential flow solution. Note that different coefficients C (see table 3) were employed for RMI with $A_1 \geq 0.5$ and $A_1 < 0.5$ to account for the effect of A_1 on asymptotic $\dot{a}_s$ (spike) and $\dot{a}_b$ (bubble). By analysing the extension of Layzer-type theory (Layzer 1955) to arbitrary A_1 (Goncharov 2002) and assuming that the linear to nonlinear growth transition occurs when $ka = 1/3$, Mikaelian (2003) proposed a nonlinear model for bubble evolution (the MIK model). Theoretically, the extension of the MIK model to spike (Goncharov 2002; Jacobs & Krivets 2005) is strictly inapplicable to RMI with finite A_1 (Mikaelian 2008). Nonetheless, it is still interesting to evaluate the capability of the MIK model to predict spike evolution because of its simplicity compared with other models (Dimonte & Ramaprabhu 2010). Through focusing on the asymptotic evolution law and the effects of A_1 and ka_0 on spike acceleration, Dimonte & Ramaprabhu (2010) proposed a nonlinear model (the DR model) applicable to high A_1 and ka_0 conditions based on numerous simulations and previous models (Zhang & Sohn 1997; Sadot *et al.* 1998; Mikaelian 2003). Zhang & Guo (2016) first derived the late-time finger (bubble and spike) growth rate for a system with any density ratio based on the finger curvature characteristics predicted by the Layzer-type models. Then, by matching the early- and late-time solutions, a nonlinear model known as the ZG model was obtained. On the basis of the ZG model, recently Zhang & Guo (2022) proposed a new nonlinear model (the ZG-New model) by considering additionally the weakly nonlinear and pre-asymptotic behaviours.

Various experimental studies have been performed to explore the nonlinear evolution law of RMI and to examine nonlinear models. In the experiments on incompressible RMI with $A_1 = -0.1587$ conducted by Niederhaus & Jacobs (2003), it was observed that the ZS (SEA) model predicts the early-time amplitude evolution well, while it underestimates (overestimates) the experimental results at later stages. The failure of the SEA model at late times was ascribed to the fact that coefficient $C = 1/2\pi$ is strictly true only when $A_1 = 0$. Using well-defined interfaces created by a membrane deposited on a stereolithographed grid support, Mariani *et al.* (2008) conducted shock-tube experiments on RMI with A_1 ranging from 0.644 to 0.721. It was observed that the predictions of the ZS and SEA models deviate from the experimental data from the early stages, which was ascribed to a part of the kinetic energy of the fluid at the interface being diverted to the motion of the membrane remnants. Subsequently, Vandenboomgaerde *et al.* (2014) studied RMI with $A_0 = 0.679$ employing an interface formation method similar to that in previous work (Mariani *et al.* 2008). A stronger incident shock was applied to reduce the deleterious effects of the membrane remnants. It was found that in the experiment with small ka_0 ($= 0.24$), the SEA (MIK) model slightly overestimates (underestimates) the amplitude evolution in the late stages, while the DR model offers a reasonable prediction. The RMI on a continuous air–SF_6 interface with $A_1 \approx 0.62$ was investigated by Collins & Jacobs (2002). It was found that the prediction of the ZS model deviates from the experimental results in the late stages, as it does not capture the late-time $1/t$ behaviour of $\dot{a}$. In contrast, the SEA model, which captures the late-time $1/t$ behaviour of $\dot{a}$, predicts the amplitude evolution well. Subsequently, Jacobs & Krivets (2005) performed experiments on the late-time development of RMI with $A_1 = 0.635$ and 0.692. Stronger shocks and initial perturbations with shorter wavelengths, in comparison to those in previous studies (Jones & Jacobs 1997; Collins & Jacobs 2002), were adopted to obtain images at significantly later dimensionless times. Jacobs & Krivets (2005) observed predictive capabilities of the ZS and SEA models similar to those in previous work (Collins & Jacobs 2002), and found that the MIK model starts underestimating the amplitude evolution from the early times, although it does capture the late-time $1/t$ behaviour of $\dot{a}$. Recently, Mansoor *et al.* (2020) studied the late-time growth of RMI on a continuous quasi-single-mode interface with $A_0 \approx 0.67$. For experiments with small ka_0 ($= 0.30$), the ZG and DR models predict reasonably the amplitude growth, while the ZS, MIK and SEA models fail to predict the experimental results well. Note that the diffusion layer of the continuous interface and the remnants of the solid membrane interface may influence the nonlinear interface evolution, thus affecting the model validation. Liu *et al.* (2018) investigated elaborately RMI on an air–SF_6 soap-film interface, and found that the ZG model predicts the amplitude growth well, while the ZS, MIK, SEA and DR models fail to predict the experimental results well in general or at specific stages. In addition, based on the accurate interface profiles extracted from high-quality schlieren pictures, modal analysis was performed. It was found that the modal model proposed by Zhang & Sohn (1997) (the ZSM model) predicts the modal evolution better than the model proposed by Vandenboomgaerde, Gauthier & Mügler (2002) (the VM model). It is noteworthy that A_1 in previous experimental works discussing nonlinear evolution of RMI (Collins & Jacobs 2002; Niederhaus & Jacobs 2003; Jacobs & Krivets 2005; Mariani *et al.* 2008; Vandenboomgaerde *et al.* 2014; Liu *et al.* 2018; Mansoor *et al.* 2020) is within a narrow range, and it is desirable to examine existing nonlinear models over a wider range of A_1.

Numerically, the evolution law of RMI has been investigated extensively (Zhou 2017*a*,*b*; Zhou *et al.* 2019, 2021). Lombardini *et al.* (2011) studied the dependence of RMI under reshock conditions on A using the large-eddy simulation technique. A wide range of A_0 in both positive and negative signs was considered: ±0.21, ±0.67 and ±0.87. The magnitude of $|A|$ was found to strongly influence the turbulent kinetic energy, turbulent dissipation and post-reshock growth rate of the mixing width. Furthermore, an empirical formula and a semi-analytical model based on a diffuse-interface approach were proposed to describe the dependence of the post-reshock growth rate on the post-reshock A. However, Lombardini *et al.* (2011) placed more emphasis on the post-reshock flow, whereas the pre-reshock classical RMI phenomenon was not highlighted. In addition to the work of Lombardini *et al.* (2011), several numerical and vortex-method-based theoretical studies of the dependence of RMI in planar and cylindrical geometries on A_1 were performed (Nishihara *et al.* 2010). Matsuoka & Nishihara (2006*a*,*b*) found that the growth rates of the bubble and spike in both planar and cylindrical geometries are closely related to A_1. Besides, the dependence of the motions, strengths and roll-up of the vortex sheet representing the interface on A_1 was discussed in detail. Existing numerical works have offered valuable insights into the evolution law of RMI under various A_1 conditions, and should be verified further through experiments. Therefore, conducting an elaborate experimental study on RMI over a wide range of A_1 conditions is desirable.

How does RMI evolve under different A_1 conditions? Can existing linear and nonlinear models describe RMI correctly over a wide range of A_1? These issues remain unclear, which motivates the present study. The soap-film technique (Liu *et al.* 2018; Liang *et al.* 2019) enables the formation of well-defined desirable interfaces, while the gas-layer scheme (Liang & Luo 2021; Chen *et al.* 2023) allows for a wide variation of A_1, providing us with a rare opportunity to study RMI over a wide range of A_1 finely through experiments. In this work, by using the soap-film technique to generate initial interfaces and the gas-layer scheme to alter A_1, first the evolution law of RMI under a wide range of A_1 conditions is obtained experimentally. Then the semi-empirical and analytical linear models and some nonlinear models are examined, and the predictive capabilities of nonlinear models are analysed and summarized. Finally, modal analysis is performed to explore the effect of A_1 on modal evolution, and also to examine modal models.

2. Experimental method

The experiments are conducted in a horizontal shock tube whose reliability and reproducibility have been verified extensively in prior investigations (Liu *et al.* 2018; Liang *et al.* 2019; Luo *et al.* 2019). The shock tube consists of a driver section, a driven section, a transitional section, a stable section and a test section, as depicted in figure 1. To generate a shock wave, initially a thin polyester film is placed between the driver and driven sections to separate the gases in them. Afterwards, nitrogen contained in a high-pressure gas cylinder is charged into the driver section. Once the pressure difference between the gases in the driver and driven sections exceeds the pressure-bearing capacity of the polyester film, the film ruptures and a shock wave is launched into the driven section. The shock wave propagates from the circular driven section to the rectangular stable section through a transitional section, and recovers to a stable one before entering the test section. In this work, the generation method of the shock wave and the thickness of the polyester film (0.03 mm) are kept consistent across all experiments, which ensures that the intensity of the shock entering the test section remains similar across different experiments.

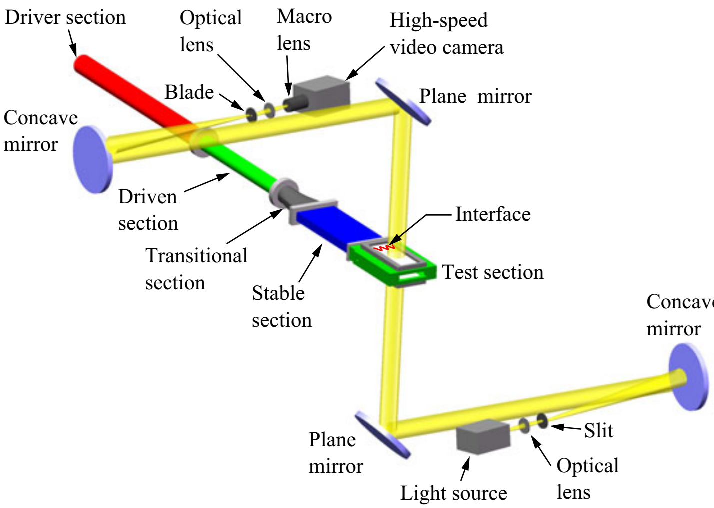

Figure 1. Sketch of the shock tube and high-speed schlieren system.

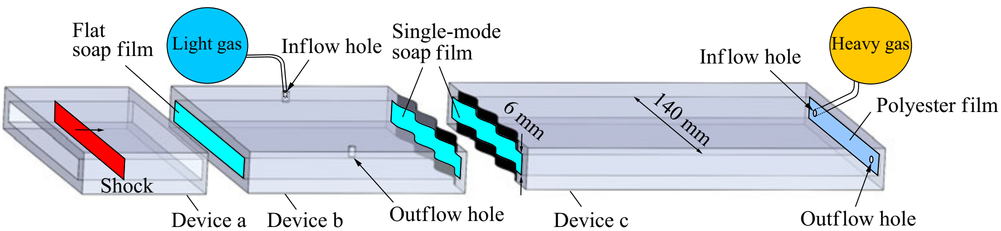

Figure 2. Schematic of interface formation devices and gas-layer scheme.

The soap-film technique, which has been utilized widely in our previous works (Liu *et al.* 2018; Liang *et al.* 2019; Luo *et al.* 2019), is used to generate the initial interface. To allow for a wider variation of A_1, it is necessary to fill different gases in the two spaces separated by the soap film. Therefore, except for the experiment with an air–SF_6 interface, a gas-layer scheme that has been validated in previous works (Liang & Luo 2021; Chen *et al.* 2023) is adopted. Before each experimental run using the gas-layer scheme, as shown in figure 2, flat and single-mode soap films are first formed on the left- and right-hand sides of device b, respectively, while a single-mode soap film is formed on the left-hand side of device c, closed with a polyester film on the right-hand side. Subsequently, gases with relatively low and high densities are charged into devices b and c, respectively, through inflow holes, and air is released through outflow holes. Finally, devices a, b and c are carefully connected and inserted into the test section of the shock tube. Note that two single-mode soap films merge into one when devices b and c are connected. Since the gas in device b (gas b) is lighter compared to that in device c (gas c), a light–heavy single-mode interface is formed. More details regarding the soap-film technique can be found in previous works (Liu *et al.* 2018; Liang *et al.* 2019).

The flow field evolution is captured by a high-speed schlieren system as depicted in figure 1. The system contains a xenon light source (CEAULIGHT CEL-HXF300), two optical lenses, a slit, two concave mirrors with a focal length of 2000 mm, two plane mirrors with a diameter of 400 mm, a blade, and a high-speed video camera (FASTCAM

Run	Gas b	Gas c	A_0	ρ_c/ρ_b	M	v_{is}^e	v_{ts}^e	v_{rs}^t	u_b^t	u^e	u^t
0.30	69 % Kr + 31 % Air	67 % SF_6 + 33 % Air	0.24	1.86	1.24	297.50	205.87	182.64	82.46	81.00	78.00
0.44	71 % Helium + 29 % Air	4 % Helium + 96 % Air	0.43	2.55	1.18	683.91	434.44	496.60	147.53	119.98	117.00
0.52	71 % Helium + 29 % Air	54 % Ar + 46 % Air	0.51	3.13	1.18	688.01	401.48	500.65	151.44	108.70	110.59
0.61	69 % Ar + 31 % Air	85 % SF_6 + 15 % Air	0.57	4.11	1.23	396.00	193.00	262.76	105.68	80.92	80.40
0.68	100 % Air	91 % SF_6 + 9 % Air	0.65	5.31	1.24	426.00	192.50	269.19	125.09	85.00	84.60
0.72	66 % Helium + 34 % Air	84 % Kr + 16 % Air	0.71	5.95	1.20	659.03	293.57	481.36	154.94	87.50	88.83
0.86	69 % Helium + 31 % Air	88 % SF_6 + 12 % Air	0.84	13.04	1.17	664.11	184.40	514.37	137.09	73.00	70.02

Table 1. Some important parameters for seven experimental runs labelled by A_1. Superscripts e and t denote experimental and theoretical results, respectively. Gases b and c are gases in devices b and c, respectively; ρ_b and ρ_c are the post-shock densities of gases b and c, respectively; M is the Mach number of the incident shock impacting the single-mode interface; v_{is}, v_{ts} and v_{rs} are the velocities of the incident, transmitted and reflected shocks, respectively; u_b is the velocity of gas b behind the incident shock; u is the shock-induced interface velocity. The unit of velocity is $\mathrm{m\,s^{-1}}$.

SA5, Photron Limited) equipped with a macro lens (TOKINA M100 PRO D 100 mm/F2.8 MACRO). The frame rate of the high-speed video camera is set to 50 000 frames per second, with an exposure time of 1 μs. The spatial resolution of schlieren images is about 0.40 mm pixel^{-1}. The ambient pressure and temperature are 101.3 ± 0.1 kPa and 295.0 ± 0.5 K, respectively.

Some important parameters for seven experimental runs labelled by A_1 are shown in table 1, and there are several issues that need further clarification. First, since the intensity of the incident shock changes as it interacts with the flat interface, there are small differences in the Mach number of the incident shock impacting the single-mode interface (M) between runs. Second, the initial distance between flat and single-mode interfaces is 105.00 mm, which ensures that the flat interface would not heavily affect the single-mode interface evolution within the effective experimental time (Chen *et al.* 2023). Third, gas components, A_0 and A_1 are obtained by matching the velocities of shocks and interface obtained from experiments and predicted by one-dimensional gas dynamics theory. Fourth, to validate the linear models and also the nonlinear models, the perturbation wavelength (λ) and ka_0 are chosen as 40.00 mm and 0.285, respectively. This ka_0 is not too small while still satisfying the small-amplitude criterion ($ka \ll 1$), which ensures that the interface has a sufficiently long linear growth period and can also evolve into the weakly nonlinear stage within the effective experimental time.

3. Results and discussion

3.1. *Flow features and interface morphology*

Experimental schlieren images of the evolutions of shocked light–heavy single-mode interfaces with different A_1 are shown in figure 3. Since the flat interface does not heavily affect the evolution of the shocked single-mode interface (SI) and provides no additional information, it is removed in all the schlieren images through image processing. Run 0.68 is taken as an example to illustrate the detailed process. The temporal origin ($t = 0$ μs) is defined as the moment when the incident shock (IS) reaches the mean position of the initial interface (II). It should be noted that the initial interface looks quite thick due to the sinusoidal filaments embedded on the interface formation devices for constraining the soap film. The filaments are also removed from the images after the shock impact through image processing for clarity. When IS encounters II, a transmitted shock (TS) and a reflected shock (RS) are generated (54 μs). Note that for runs in which gas b is a mixture of helium and air, RS is barely visible since the difference in gas density between its two sides is small. As SI evolves, its asymmetry increases gradually, followed by the formation of distinct spike and bubble structures (674 μs), indicating the generation of high-order harmonics. Subsequently, roll-up structures are formed on SI (1114 μs).

The nonlinear evolution features of SI, including spike, bubble and roll-up structures, develop faster in RMI with higher A_1. Specifically, before moving out of the experimental observation area, SI in run 0.30 remains a quasi-single-mode profile (1123 μs), while SI in run 0.86 becomes highly asymmetrical and has roll-up structures (1103 μs). Notably, Matsuoka & Nishihara (2006*a*) observed that the roll-up structures of RMI in cylindrical geometry appear rapidly even under low A_1 conditions, which appears to be inconsistent with the present results. However, this discrepancy is due to the difference in time normalization between RMI in planar and cylindrical geometries. In the studies conducted by Matsuoka & Nishihara (2006*b*) and Nishihara *et al.* (2010) on RMI in planar geometry, using the same time normalization as that in the current work (see § 3.3 for details), the

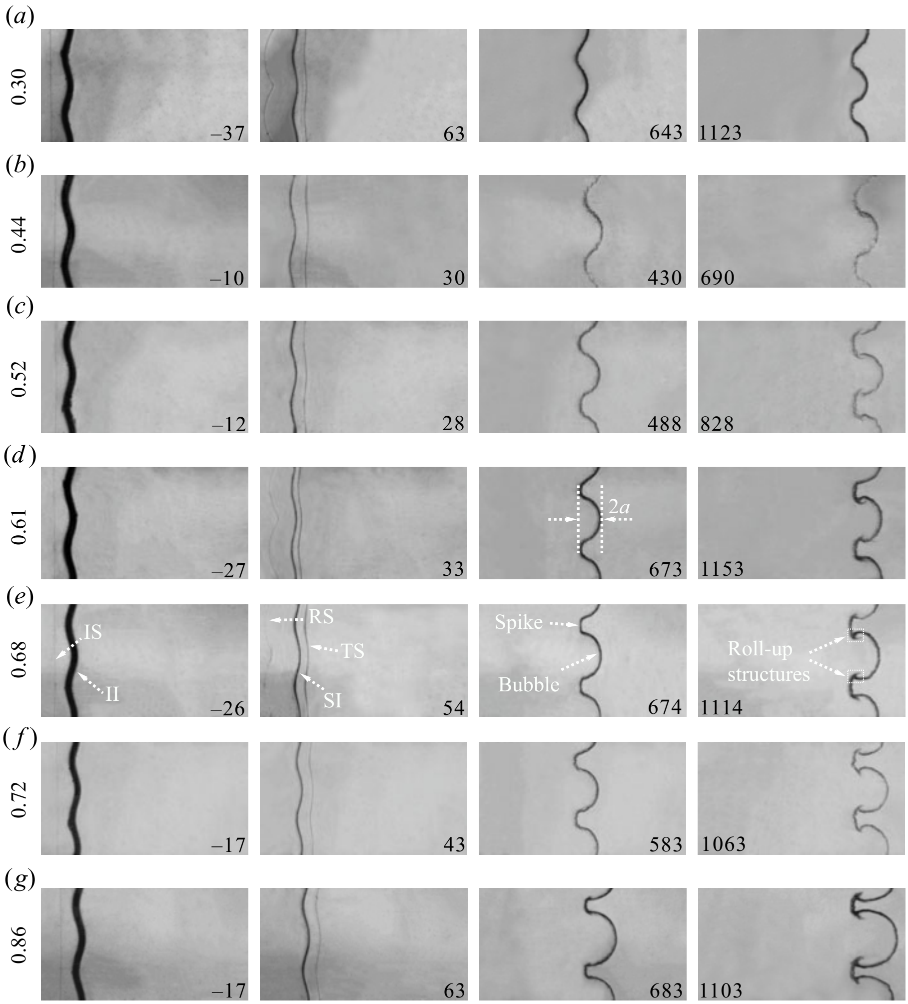

Figure 3. Schlieren photographs of the evolutions of shocked interfaces with different A_1. Here, IS, TS and RS denote incident, transmitted and reflected shocks, respectively; II and SI denote initial and shocked single-mode interfaces, respectively. Numbers in photographs represent time in μs.

roll-up structures have not yet emerged when the dimensionless time reaches 2 under low A_1 conditions. This observation aligns with the phenomenon witnessed in our experiments.

3.2. *Linear evolution of perturbation amplitude*

Temporal variations of perturbation amplitude a in dimensional form for different runs are shown in figure 4(a), in which t^* is the moment when the linear growth of a starts, and a^* is the corresponding a at $t = t^*$. Note that a is determined via measuring the distance between the peak and trough of SI along the streamwise direction ($2a$), as shown in figure 3. In all runs, a would initially undergo a linear growth period, and $\dot{a}_1^e$ is determined by linearly fitting the early-time experimental data. According to previous works (Mikaelian 1994; Yang *et al.* 1994; Velikovich & Dimonte 1996), the impulsive model is valid theoretically for predicting $\dot{a}_1$ only when ka_0 is small and compressibility is weak. In the experiments conducted in this work, ka_0 satisfies the small-amplitude

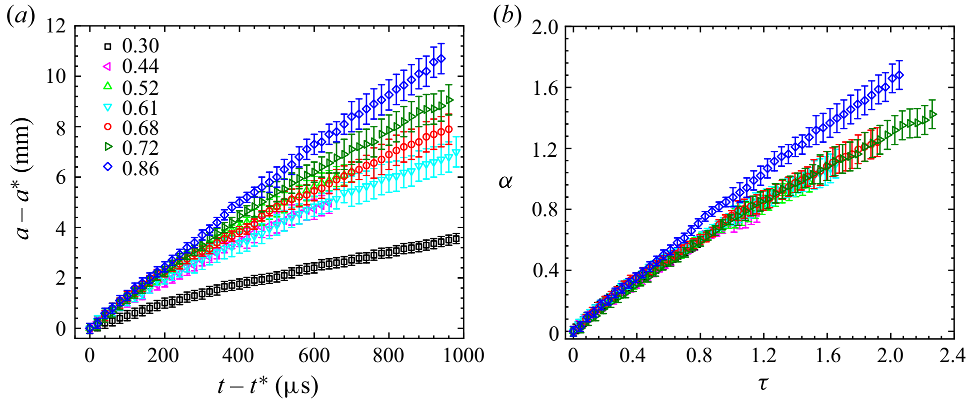

Figure 4. Temporal variations of perturbation amplitude for runs with different A_1: (*a*) dimensional form, (*b*) dimensionless form.

criterion and M is low. Therefore, our experiments are suitable for validating the impulsive model, which can be written as

$$\dot{a}_1^i = Cka_0A_1u^t = ka_1A_1u^t, \tag{3.1}$$

where C $(= 1 - u^t/v_{is}^e)$ is the shock compression factor, with u^t and v_{is}^e being the theoretical velocity of SI and the experimental velocity of IS, respectively, and a_1 is the post-shock amplitude. In addition to the semi-empirical impulsive model, it is also desirable to examine the analytical linear models (Wouchuk & Nishihara 1996, 1997; Wouchuk 2001). According to Wouchuk & Nishihara (1997), the difference between the predictions of the WN and WN-WL models is negligible when $\beta < 0.5$ (where $\beta = 1 - p_{in}/p_{be}$, in which p_{in} and p_{be} are the pressures in front of and behind IS, respectively). Since β in current experiments are smaller than 0.4, only the WN-WL model is considered. The WN-WL model can be expressed as

$$\dot{a}_1^{ww} = ka_0 \frac{u^t \dfrac{\rho_c}{\rho_b}\left(1 - \dfrac{v_{ts}^e}{v_{is}^e}\right) + (u_b^t - u^t)\left(1 + \dfrac{v_{rs}^t}{v_{is}^e}\right)}{1 + \dfrac{\rho_c}{\rho_b}}, \tag{3.2}$$

where ρ_b and ρ_c are the post-shock densities of gases b and c, respectively; v_{ts}^e is the velocity of TS extracted from experiments; and v_{rs}^t and u_b^t are the velocities of RS and gas b behind IS predicted by one-dimensional gas dynamics theory, respectively. To demonstrate more visually the dependence of $\dot{a}_1$ on A_1 described by the WN-WL model, the model can be rewritten as

$$\dot{a}_1^{ww} = ka_0\left[\frac{1 + A_1}{2}u^t\left(1 - \frac{v_{ts}^e}{v_{is}^e}\right) + \frac{1 - A_1}{2}(u_b^t - u^t)\left(1 + \frac{v_{rs}^t}{v_{is}^e}\right)\right]. \tag{3.3}$$

Values of $\dot{a}_1^e$, $\dot{a}_1^i$ and $\dot{a}_1^{ww}$ are provided in table 2 for comparison. It can be found that the impulsive model predicts excellently $\dot{a}_1^e$ under a wide range of A_1 conditions, while the WN-WL model provides reasonable predictions for all experimental results. The result of the comparison indicates that both models describe correctly the dependence of the linear amplitude evolution on A_1.

Run	0.30	0.44	0.52	0.61	0.68	0.72	0.86
$\dot{a}_1^e$ (m s^{-1})	4.87 ± 0.13	11.51 ± 0.61	13.52 ± 0.98	10.75 ± 0.43	12.70 ± 0.30	15.00 ± 0.58	13.91 ± 1.48
$\dot{a}_1^i$ (m s^{-1})	4.93	12.03	13.66	11.10	13.19	15.55	15.30
$\dot{a}_1^{ww}$ (m s^{-1})	5.15	13.00	14.79	11.79	14.14	16.70	15.81

Table 2. Comparison of linear asymptotic amplitude growth rates $\dot{a}_1$ obtained from experiments ($\dot{a}_1^e$) and predicted by the impulsive model ($\dot{a}_1^i$) and the WN-WL model ($\dot{a}_1^{ww}$).

Model	Expression
ZS	$\dot{a}^{zs}_{b/s} = \dot{a}^{zs} \mp \dfrac{A_1 k \dot{a}^{e\,2}_1 t}{1 + 2k^2 \dot{a}^e_1 a_1 t + 4k^2 \dot{a}^{e\,2}_1 t^2 \left[a^2_1 k^2 + \frac{1}{3}(1 - A^2_1)\right]}$, in which $\dot{a}^{zs} = \dfrac{\dot{a}^e_1}{1 + k^2 \dot{a}^e_1 a_1 t + \max\left[0, k^2 a^2_1 - A^2_1 + \frac{1}{2}\right] k^2 \dot{a}^{e\,2}_1 t^2}$.
MIK	$\dot{a}^{mik}_{b/s} = \dot{a}^e_1$ when $ka < 1/3$, $\dot{a}^{mik}_{b/s} = \dfrac{\dot{a}^e_1}{1 + 3\dot{a}^e_1 \left(\dfrac{1 \pm A_1}{3 \pm A_1}\right) kt}$ when $ka \geq 1/3$.
SEA	$\dot{a}^{sea}_{b/s} = \dot{a}^e_1 \dfrac{1 + k\dot{a}^e_1 t}{1 + (1 \pm A_1) k \dot{a}^e_1 t + \left(\dfrac{1 \pm A_1}{1 + A_1}\right)\left(\dfrac{k^2 \dot{a}^{e\,2}_1 t^2}{2\pi C}\right)}$, in which $C = \dfrac{1}{3\pi}$ when $A_1 \geq 0.5$ and $C = \dfrac{1}{2\pi}$ when $A_1 \to 0$.
DR	$\dot{a}^{dr}_{b/s} = \dot{a}^e_1 \dfrac{1 + (1 \mp A_1) k \dot{a}^e_1 t}{1 + C_{b/s} k \dot{a}^e_1 t + (1 \mp A_1) F_{b/s} (k \dot{a}^e_1 t)^2}$, in which $C_{b/s} = \dfrac{4.5 \pm A_1 + (2 \mp A_1) k a_1}{4}$ and $F_{b/s} = 1 \pm A_1$.
ZG	$\dot{a}^{zg}_{b/s} = \dfrac{\dot{a}^e_1}{1 + \theta_{b/s} k \dot{a}^e_1 t}$, in which $\theta_{b/s} = \dfrac{3}{4} \dfrac{(1 \pm A_1)(3 \pm A_1)}{3 \pm A_1 + \sqrt{2(1 \pm A_1)}} \dfrac{4(3 \pm A_1) + \sqrt{2}(9 \pm A_1)(1 \pm A_1)^{1/2}}{(3 \pm A_1)^2 + 2\sqrt{2}(3 \mp A_1)(1 \pm A_1)^{1/2}}$.
ZG-New	$\dot{a}^{zgn}_{b/s} = \dot{a}^e_1\, \mathrm{e}^{-k[a_{b/s}(t) - a_1]\theta_{b/s}} \left\{ \dfrac{\dfrac{1}{3(\theta_{b/s} \mp A_1)^2}\left(1 + \dfrac{2ka_1}{\theta_{b/s} \mp A_1}\right) + \lambda_{b/s}}{\dfrac{1}{3(\theta_{b/s} \mp A_1)^2}\left(1 + \dfrac{2ka_1}{\theta_{b/s} \mp A_1}\right) + \lambda_{b/s}\, \mathrm{e}^{-3k[a_{b/s}(t) - a_1]}} \right\}^{1/3\lambda_{b/s}}$, in which $\lambda_{b/s} = \left[\dfrac{1}{\theta_{b/s} \mp A_1} - \dfrac{1}{3(\theta_{b/s} \mp A_1)^2}\right] + \left[\dfrac{1}{(\theta_{b/s} \mp A_1)^2} - \dfrac{2}{3(\theta_{b/s} \mp A_1)^3}\right] k a_1$.

Table 3. Detailed expressions of considered nonlinear models.

3.3. *Weakly nonlinear evolution of perturbation amplitude*

Temporal variations of perturbation amplitude a in dimensionless form for runs with different A_1 are shown in figure 4(*b*). Here, t and a are normalized as $\tau = k\dot{a}^e_1(t - t^*)$ and $\alpha = k(a - a^*)$, respectively, where τ values corresponding to the last data point (τ_l) in different runs are in the range 0.7–2.3. Therefore, SI in all runs can be considered to be within the weakly nonlinear evolution stage at $\tau = \tau_l$. The scaling collapses the results of all runs except run 0.86, indicating that the weakly nonlinear evolution law of RMI with A_1 close to 1 is significantly different from that of RMI with relatively low A_1. Then a comparative analysis of experimental results and predictions by typical nonlinear models is performed. Nonlinear models including the ZS, MIK, SEA, DR, ZG and ZG-New models are considered, and their detailed expressions are listed in table 3. From the comparison of the experimental and theoretical results, we notice that the predictive capabilities of considered nonlinear models for runs 0.30, 0.44 and 0.52 (runs 0.61, 0.68 and 0.72) are similar. Therefore, for clarity, three typical experiments (runs 0.30, 0.68 and 0.86), referred

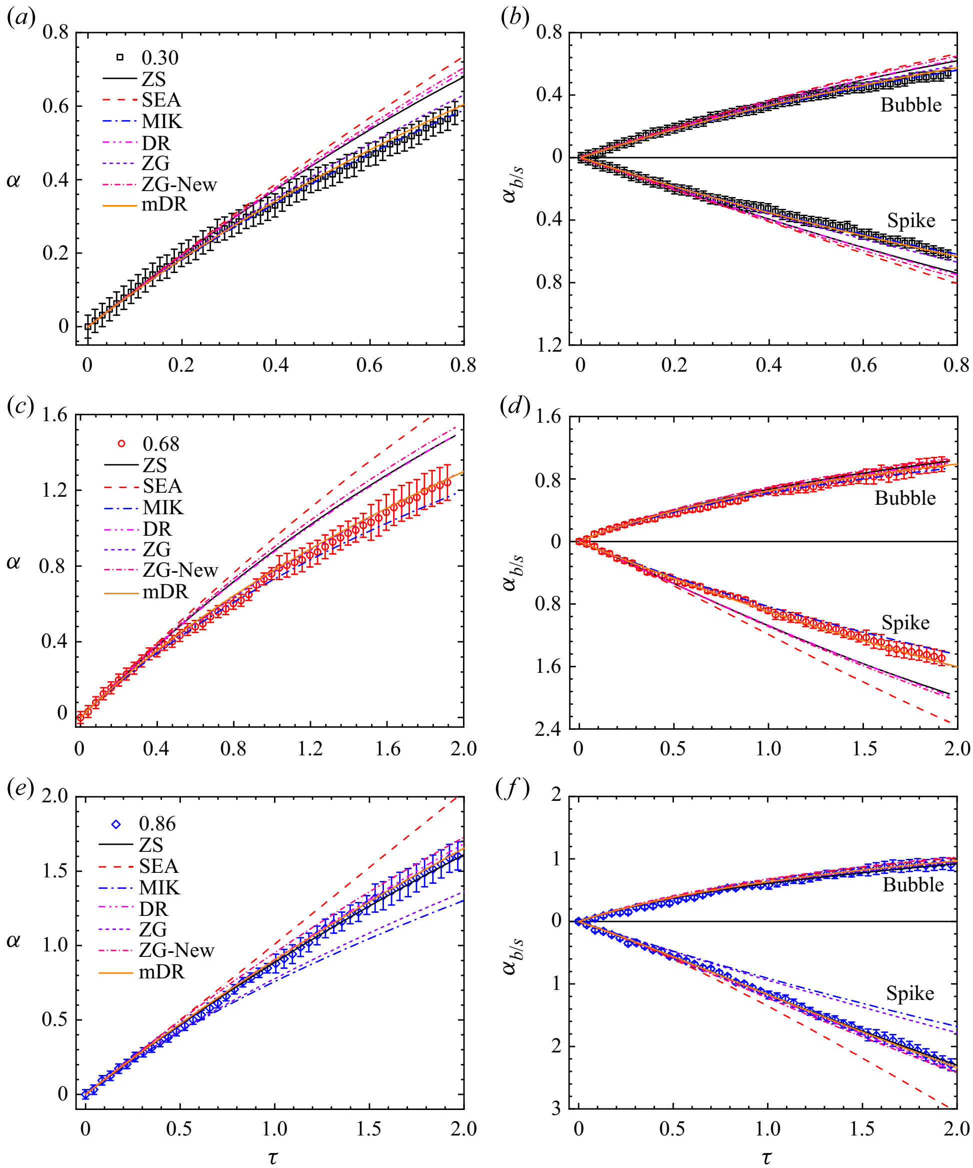

Figure 5. Comparisons between experimental and theoretical results for (*a*,*c*,*e*) dimensionless a and (*b*,*d*,*f*) dimensionless $a_{b/s}$, for (*a*,*b*) run 0.30, (*c*,*d*) run 0.68, and (*e*,*f*) run 0.86.

to below as RMI with low, intermediate and high A_1, respectively, are chosen for further discussion.

The temporal variations of a and $a_{b/s}$ (where subscripts b and s represent bubble and spike, respectively) in dimensionless form obtained from experiments and predicted by nonlinear models for runs 0.30, 0.68 and 0.86 are shown in figure 5. For run 0.30, the MIK (ZG) model excellently (reasonably) predicts the experimental results, while the other models slightly overestimate a and $a_{b/s}$. For run 0.68, the ZG model provides the best prediction of the experimental results, while the MIK model slightly underestimates a and a_s at late stages. The ZS, SEA, DR and ZG-New models well predict a_b while obviously overestimating a and a_s. In run 0.86, $\dot{a}_s$, which decreases continuously in RMI with low or intermediate A_1, increases gradually, verifying the numerical observation that the spike acceleration is significant when A_1 is high (Dimonte & Ramaprabhu 2010). The SEA model (MIK and ZG models) obviously overestimates (underestimate) a and a_s while still predicting (forecasting) a_b well. In contrast, the ZS, DR and ZG-New models also predict a and a_s well. Notably, the significant spike acceleration phenomenon is observed experimentally for the first time.

Before analysing the predictive capabilities of nonlinear models, it is important to mention that even if the experimental and theoretical results agree well, it may be accidental. For example, as observed by Dimonte & Ramaprabhu (2010), the MIK model, which is theoretically inapplicable when $ka_1 > 1/3$, reasonably predicts the numerical results with $ka_1 \approx 1$. All considered models can reasonably predict the bubble evolution under a wide range of A_1 conditions, probably because the bubble is more stable than spike, and its asymptotic curvature is insensitive to A_1 (Zhang & Guo 2022). In the following, we will focus on the predictive capabilities of models for the evolutions of a and a_s.

ZS model: asymptotic $\dot{a}$ predicted by the ZS model satisfies the $1/t^2$ law when $A_1 < \sqrt{1/2 + (ka_1)^2} \approx 0.75$ and the $1/t$ law when $A_1 > \sqrt{1/2 + (ka_1)^2} \approx 0.75$. Note that the late-time $1/t$ law of $\dot{a}$ is expected from the potential flow model and has been validated in previous numerical and experimental works (Dimonte & Ramaprabhu 2010; Mansoor *et al.* 2020). Thus the ZS model fails to predict a and a_s well for runs 0.30 and 0.68, while reasonably predicting the results of run 0.86.

SEA model: the overestimation of the SEA model for a and a_s under various A_1 conditions should be ascribed to its overestimation of the spike acceleration (Dimonte & Ramaprabhu 2010).

MIK model: the extension of the MIK model to spike is realized using Goncharov's method (Goncharov 2002), and Goncharov's method is based on the assumption that the asymptotic curvatures of spike and bubble are equal. Besides, the MIK model includes no term describing spike acceleration. When A_1 is low, the assumption of Goncharov's method is reasonable (Zhang & Guo 2022), and the spike acceleration should be absent or very weak. Therefore, the MIK model predicts the weakly nonlinear evolution of RMI with low A_1 well. Since the asymptotic curvature of spike is sensitive to A_1 (Mikaelian 2008; Zhang & Guo 2022), the assumption of Goncharov's method is no longer reasonable when A_1 is intermediate or high. In other words, the MIK model is theoretically inapplicable to predict the spike evolution of RMI with intermediate or high A_1. Therefore, the relatively good prediction of RMI with intermediate A_1 by the MIK model may be accidental. The spike acceleration is significant when A_1 is high, therefore the MIK model obviously underestimates a and a_s for run 0.86.

DR model: the purpose of Dimonte & Ramaprabhu (2010) was to develop an empirical nonlinear model applicable to RMI with high A_1 and ka_0 conditions. Therefore, although numerical simulations with low and intermediate A_1 were also considered when constructing the DR model, more emphasis was placed on achieving a good match between model predictions and numerical results of RMI with high A_1. Accordingly, the poor predictive capability of the DR model for runs 0.30 and 0.68, and its good predictive capability for run 0.86, are reasonable and expected.

ZG and ZG-New models: the similarities and differences between these two models can be summarized in three parts. First, compared to the ZG model, the ZG-New model considers two additional physical processes, i.e. the weakly nonlinear process and the pre-asymptotic process. Therefore, whether for RMI with low, intermediate or high A_1, the ZG-New model is theoretically more accurate than the ZG model. Second, in the early

A_1	Amplitude	ZS	SEA	MIK	DR	ZG	ZG-New
Low	Overall interface	✗	✗	✓	✗	●	✗
	Bubble	✗	✗	✓	✗	✓	✗
	Spike	✗	✗	✓	✗	●	✗
Intermediate	Overall interface	✗	✗	●	✗	●	✗
	Bubble	✓	✓	✓	✓	✓	✓
	Spike	✗	✗	●	✗	●	✗
High	Overall interface	✓	✗	✗	✓	✗	✓
	Bubble	✓	✓	✓	✓	✓	✓
	Spike	✓	✗	✗	✓	✗	✓

Table 4. Summary of the predictive capabilities of considered nonlinear models for the amplitude evolutions of the overall interface, bubble and spike under different A_1 conditions. Here, ✓ indicates that the model is applicable both theoretically and practically, ● indicates that the model is theoretically inapplicable but accidentally applicable in practice, and ✗ indicates that the model is practically inapplicable.

stages, the ZG and ZG-New models recover to the small-time behaviours predicted by the linear and ZS models, respectively. In other words, the ZG-New model (ZG model) considers (does not consider) the spike acceleration. Third, in the asymptotic stages, both models recover to the late-time solution proposed based on several properties observed from a potential flow system with infinite density ratio ($A_1 = \pm 1$). Therefore, both models should be more accurate for RMI with high A_1 than for RMI with low or intermediate A_1. The ZG-New model overestimates the results of RMI with low or intermediate A_1, which should be attributed to the limitation of the late-time solution. The ZG model ignores the weakly nonlinear and pre-asymptotic processes, and its late-time solution may be not very accurate when A_1 is low or intermediate. Therefore, the relatively good prediction of RMI with low or intermediate A_1 by the ZG model should be accidental. When A_1 is high, the spike acceleration is significant and the late-time solution on which the ZG and ZG-New models are based is theoretically more reasonable. Therefore, the ZG-New model predicts the results of run 0.86 well, while the ZG model, which ignores spike acceleration, underestimates a and a_s in this case.

The predictive capabilities of considered nonlinear models for the amplitude evolutions of the overall interface, bubble and spike under different A_1 conditions are summarized in table 4. None of the considered models is applicable to RMI under all A_1 conditions. Since the interface evolution studied in the present work is limited to weakly nonlinear stage, the failure of models should be attributed mainly to the insufficient description of the dependence of the spike acceleration on A_1. A rigorous description of the spike acceleration under various A_1 conditions is rather difficult, therefore we attempt to propose an empirical model applicable to RMI over a wide range of A_1 based on the present experimental results. The DR model not only considers the spike acceleration occurring in the early stages and captures the late-time $1/t$ behaviour of $\dot{a}$, but also describes the effect of ka_0 on nonlinear evolution law. Therefore, we will construct a new empirical model (the mDR model) by modifying the DR model. The mDR model obtained after many attempts can be written as

$$\dot{a}_{b/s}^{mdr} = \dot{a}_1^e \frac{1 + E(1 \mp A_1)k\dot{a}_1^e t}{1 + C_{b/s}k\dot{a}_1^e t + E(1 \mp A_1)F_{b/s}(k\dot{a}_1^e t)^2}, \tag{3.4}$$

in which $E = (3 - 2A_1)/(9 - 9A_1)$. The introduction of the coefficient E, which is smaller than 1 when A_1 is low or intermediate, solves the problem that the DR model overestimates

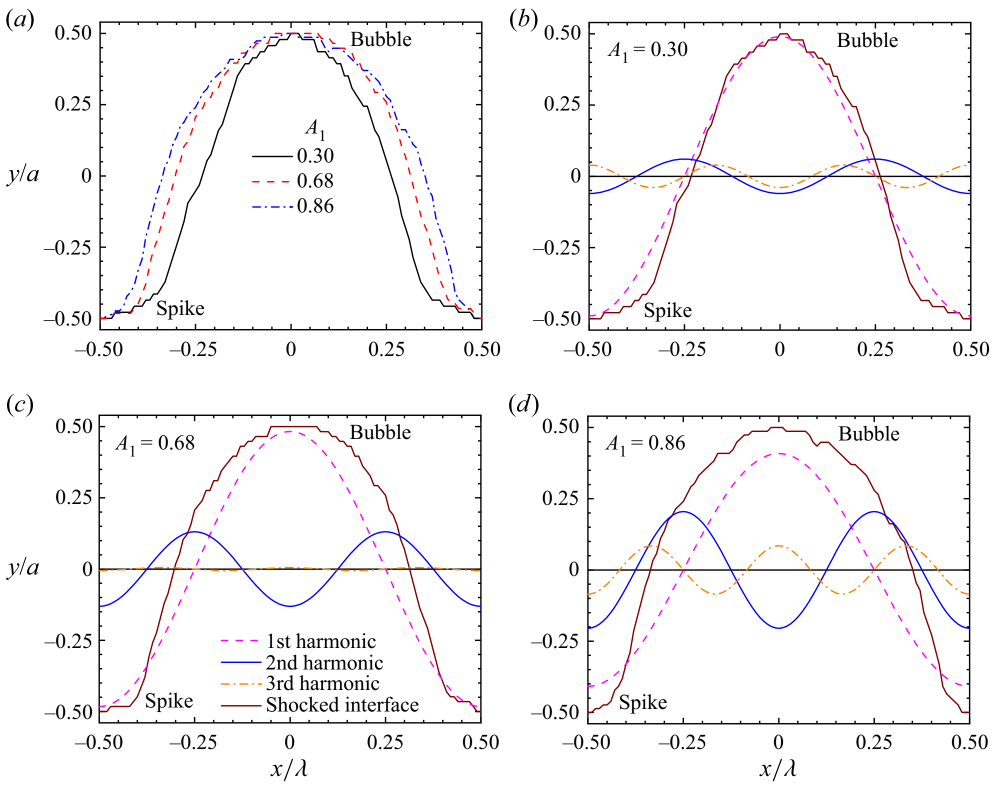

Figure 6. (*a*) Comparison of dimensionless contours of SI at $\tau \approx 0.7$ obtained from different runs. Modal information of the contour of SI at $\tau \approx 0.7$: (*b*) run 0.30, (*c*) run 0.68, and (*d*) run 0.86.

spike acceleration under low and intermediate A_1 conditions. When $A_1 \rightarrow 0.86$, $E \rightarrow 1$, i.e. the mDR model recovers to the DR model, which ensures that the mDR model can also predict well RMI with high A_1. Besides, the mDR model can also recover to the DR model in the asymptotic stages. Note that although the mDR model is invalid when A_1 approaches 1 due to the limitation of E, it is capable of predicting the amplitude evolution of RMI with A_1 ranging from 0.30 to 0.86 as shown in figure 5.

3.4. *Modal evolution in the weakly nonlinear stage*

Modal analysis is performed to explore the modal evolution under various A_1 conditions. Similarly, three typical experiments (runs 0.30, 0.68 and 0.86) are considered for clarity. The fast Fourier transform (FFT) is applied to obtain the modal information of the interface. Because the FFT is applicable only when the interface profile can be described by a single-valued function (Wang *et al.* 2022), only the modal evolution prior to the formation of roll-up structures is investigated. In addition, since the modal analysis is limited to the weakly nonlinear stage, the magnitudes of the fourth-order and other higher-order harmonics are very small relative to that of the first harmonic, therefore only the first three harmonics (m_1, m_2 and m_3) are considered (Liu *et al.* 2018).

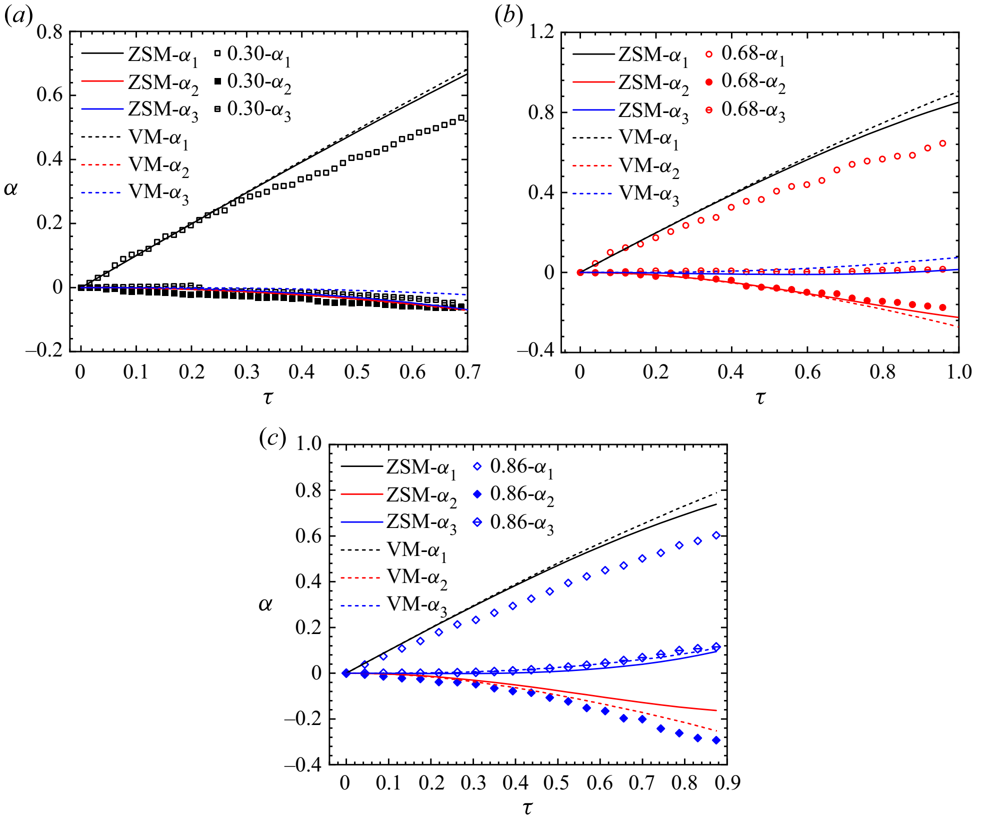

Figure 7. Modal evolutions obtained from experiments and predicted by modal models: (*a*) run 0.30, (*b*) run 0.68, and (*c*) run 0.86.

3.4.1. *Effect of modal evolution on interface morphology*

The dimensionless contours of shocked interface SI at $\tau \approx 0.7$ obtained from runs with different A_1 are provided in figure 6(*a*). Here, $x = 0$ and $y = 0$ correspond to the x-coordinate of the bubble tip and the y-coordinate of the middle position between bubble and spike tips, respectively. It can be noticed that SI in run 0.30 remains almost symmetrical, and the asymmetry of SI is higher in RMI with higher A_1.

Modal information of the SI contours shown in figure 6(*a*) is obtained by FFT and presented in figures 6(*b–d*). For run 0.30, the dimensionless amplitudes of m_2 and m_3 (α_2 and α_3) are still significantly smaller than that of m_1 (α_1) at $\tau \approx 0.7$, therefore SI maintains an almost symmetrical shape. For run 0.68, α_2 increases to a considerable level when $\tau \approx 0.7$. Considering only the right half of SI, i.e. SI with x/λ ranging from 0 to 0.5, m_1 and m_2 have the same phase at positions close to the spike tip ($0.375 < x/\lambda < 0.5$) and in the range $0.125 < x/\lambda < 0.25$. In contrast, m_1 and m_2 have opposite phases at positions close to the bubble tip ($0 < x/\lambda < 0.125$) and in range $0.25 < x/\lambda < 0.375$. Therefore, m_2 tends to flatten the bubble (Guo *et al.* 2020) and sharpen the spike, resulting in a significant asymmetry of the SI in run 0.68. For run 0.86, α_3 also increases to a considerable level when $\tau \approx 0.7$. Here, m_2 and m_3 have opposite phases at positions close to the bubble tip ($0 < x/\lambda < 0.083$) and have the same phase at positions close to the spike tip ($0.417 < x/\lambda < 0.5$). In other words, m_2 and m_3 have opposite contributions to the flatness of the bubble, while together promoting the sharpening of the spike. Therefore, the spike profile in run 0.86 is obviously different from that in run 0.68, while the difference in bubble profile between these two runs is less pronounced.

3.4.2. *Model validation and analysis*

Evolutions of α_1, α_2 and α_3 obtained from experiments and predicted by modal models for runs 0.30, 0.68 and 0.86 are shown in figure 7. For run 0.30, both α_2 and α_3 grow very slowly. The ZSM and VM models have limited effective range, and their accuracies are sensitive to ka (Jacobs & Krivets 2005) since they are both derived by the perturbation expansion method. Thus the ZSM and VM models predict α_1 well (poorly) when $\alpha_1 < 0.3$ ($\alpha_1 > 0.3$). The predictions of the ZSM and VM models for α_2 are similar and agree with the experimental results. In the late stages, the predictions of the ZSM and VM models for α_3 differ slightly, and both deviate slightly from the experimental results.

For run 0.68, α_3 still varies very slowly and remains far smaller than α_1 from early to late stages. In contrast, α_2 grows to a considerable level in the late stages. The predictions of the ZSM and VM models for α_1 are similar and agree well (poorly) with the experimental results when $\alpha_1 < 0.2$ ($\alpha_1 > 0.2$). The ZSM model considers only the contributions of the first fourth-order perturbation solutions, whereas the VM model accounts for perturbation solutions up to 11th-order, but with an additional simplification: only the terms with the highest power in t are retained. Therefore, when high-order harmonics can (cannot) be ignored, the ZSM model should be more (less) accurate than the VM model. In run 0.68, m_3 is negligible and, accordingly, the higher-order harmonics should also be negligible. Therefore, the ZSM model predicts α_2 and α_3 in run 0.68 better than the VM model.

In run 0.86, m_2 (m_3) develops obviously faster than those in runs 0.30 and 0.68, and becomes considerable in the late stages. The predictions of the ZSM and VM models for α_1 are similar and agree well (poorly) with the experimental results when $\alpha_1 < 0.1$ ($\alpha_1 > 0.1$). It can be noticed that the predictive capabilities of the ZSM and VM models for α_1 are also related to A_1. For α_2 (α_3), the VM model instead of the ZSM model provides a better prediction in the late stages, validating the above analysis that the VM model should be more accurate than the ZSM model when high-order harmonics are no longer negligible.

4. Conclusions

Richtmyer–Meshkov instability (RMI) on a light–heavy single-mode interface over a wide range of post-shock Atwood numbers (A_1) is studied finely and systematically through experiments. To perform experiments under a wide range of A_1 conditions, in addition to the soap-film technique, which can produce well-defined desirable interfaces, a gas-layer scheme is adopted such that the spaces on both sides of the soap film can be filled with different gases.

Qualitatively, the nonlinear evolution features of the shocked interface (SI), including spike, bubble and roll-up structures, are more significant in RMI with higher A_1. Specifically, before moving out of the experimental observation area, SI in RMI with low A_1 remains a quasi-single-mode profile, while SI in RMI with high A_1 becomes highly asymmetrical and has roll-up structures. Quantitatively, the impulsive model (Richtmyer 1960) and the WN-WL model (Wouchuk & Nishihara 1997) are found to be valid for predicting the linear growth rate under a wide range of A_1 conditions, indicating that both models describe correctly the dependence of the linear amplitude evolution on A_1. For the weakly nonlinear evolution stage, the significant spike acceleration (occurring when

A_1 is high) results in the evolution law of RMI with high A_1 being different from that of RMI with low or intermediate A_1. Notably, the significant spike acceleration phenomenon is observed experimentally for the first time. None of the considered nonlinear models (Zhang & Sohn 1997; Sadot *et al.* 1998; Mikaelian 2003; Dimonte & Ramaprabhu 2010; Zhang & Guo 2016, 2022) is found to apply to RMI under all A_1 conditions, and the predictive capabilities of these models are analysed and summarized. Based on the present experimental results, an empirical nonlinear model applicable to RMI over a wide range of A_1 is proposed. Further, modal analysis shows that the second harmonic tends to flatten the bubble and sharpen the spike, while the third harmonic tends to sharpen both bubble and spike. In RMI with high (low or intermediate) A_1, high-order harmonics evolve rapidly (slowly) and cannot (can) be ignored. Accordingly, for RMI with high (low or intermediate) A_1, the modal model proposed by Zhang & Sohn (1997) is less (more) accurate than the model proposed by Vandenboomgaerde *et al.* (2002), since the former ignores perturbation solutions higher than fourth order (the latter retains only terms with the highest power in time).

In inertial confinement fusion (ICF), the development of spike can lead to ablative material entering the hot spot, which would substantially reduce the energy gain and even lead to ignition failure (Kritcher *et al.* 2022). According to the present work, to avoid the intense spike development occurring when A_1 is high, we discreetly suggest choosing ablative material with relatively low density to reduce the density ratio between ablator and deuterium-tritium (DT) ice. In addition, it is important to note that in ICF, the interface separating ablator and DT ice, and the interface separating DT ice and DT gas, are both heavy–light. Therefore, investigating RMI on a heavy–light interface over a wide range of A_1 is also necessary and interesting, as discussed by Lombardini *et al.* (2011). A relevant work is currently ongoing. Fortunately, due to the flexibility of the gas-layer scheme – i.e. gases on both sides of the soap film can be altered as desired – experiments on RMI with diverse negative A_1 can be conducted without changing the structure of the shock-tube facility adopted in the present work.

Funding. This work was supported by the National Natural Science Foundation of China (nos 12102425, 12022201 and 91952205) and Youth Innovation Promotion Association CAS.

Declaration of interests. The authors report no conflict of interest.

Author ORCIDs.
He Wang https://orcid.org/0000-0002-6497-6673;
Zhigang Zhai https://orcid.org/0000-0002-0094-5210;
Xisheng Luo https://orcid.org/0000-0002-4303-8290.

REFERENCES

ARNETT, W.D., BAHCALL, J.N., KIRSHNER, R.P. & WOOSLEY, S.E. 1989 Supernova 1987A. *Annu. Rev. Astron. Astrophys.* **27**, 629–700.

BETTI, R. & HURRICANE, O.A. 2016 Inertial-confinement fusion with lasers. *Nat. Phys.* **12**, 435–448.

BILLIG, F.S. 1993 Research on supersonic combustion. *J. Propul. Power* **9**, 499–514.

CHEN, C., XING, Y., WANG, H., ZHAI, Z. & LUO, X. 2023 Freeze-out of perturbation growth of single-mode helium–air interface through reflected shock in Richtmyer–Meshkov flows. *J. Fluid Mech.* **956**, R2.

COLLINS, B.D. & JACOBS, J.W. 2002 PLIF flow visualization and measurements of the Richtmyer–Meshkov instability of an air/SF_6 interface. *J. Fluid Mech.* **464**, 113–136.

DIMONTE, G. & RAMAPRABHU, P. 2010 Simulations and model of the nonlinear Richtmyer–Meshkov instability. *Phys. Fluids* **22**, 014104.

GONCHAROV, V.N. 2002 Analytical model of nonlinear, single-mode, classical Rayleigh–Taylor instability at arbitrary Atwood numbers. *Phys. Rev. Lett.* **88**, 134502.

GUO, X., ZHAI, Z., DING, J., SI, T. & LUO, X. 2020 Effects of transverse shock waves on early evolution of multi-mode chevron interface. *Phys. Fluids* **32**, 106101.
JACOBS, J.W. & KRIVETS, V.V. 2005 Experiments on the late-time development of single-mode Richtmyer–Meshkov instability. *Phys. Fluids* **17**, 034105.
JONES, M.A. & JACOBS, J.W. 1997 A membraneless experiment for the study of Richtmyer–Meshkov instability of a shock-accelerated gas interface. *Phys. Fluids* **9**, 3078–3085.
KHOKHLOV, A.M., ORAN, E.S., CHTCHELKANOVA, A.Y. & WHEELER, J.C. 1999*a* Interaction of a shock with a sinusoidally perturbed flame. *Combust. Flame* **117**, 99–116.
KHOKHLOV, A.M., ORAN, E.S. & THOMAS, G.O. 1999*b* Numerical simulation of deflagration-to-detonation transition: the role of shock–flame interactions in turbulent flames. *Combust. Flame* **117**, 323–339.
KRITCHER, A.L., *et al.* 2022 Design of inertial fusion implosions reaching the burning plasma regime. *Nat. Phys.* **18**, 251–258.
KURANZ, C.C., *et al.* 2018 How high energy fluxes may affect Rayleigh–Taylor instability growth in young supernova remnants. *Nat. Commun.* **9**, 1564.
LAYZER, D. 1955 On the instability of superposed fluids in a gravitational field. *Astrophys. J.* **122**, 1–12.
LIANG, Y. & LUO, X. 2021 On shock-induced heavy-fluid-layer evolution. *J. Fluid Mech.* **920**, A13.
LIANG, Y., ZHAI, Z., DING, J. & LUO, X. 2019 Richtmyer–Meshkov instability on a quasi-single-mode interface. *J. Fluid Mech.* **872**, 729–751.
LINDL, J. 1995 Development of the indirect-drive approach to inertial confinement fusion and the target physics basis for ignition and gain. *Phys. Plasmas* **2**, 3933–4024.
LINDL, J., LANDEN, O., EDWARDS, J., MOSES, E. & N.I.C. TEAM 2014 Review of the national ignition campaign 2009–2012. *Phys. Plasmas* **21**, 020501.
LIU, L., LIANG, Y., DING, J., LIU, N. & LUO, X. 2018 An elaborate experiment on the single-mode Richtmyer–Meshkov instability. *J. Fluid Mech.* **853**, R2.
LOMBARDINI, M., HILL, D.J., PULLIN, D.I. & MEIRON, D.I. 2011 Atwood ratio dependence of Richtmyer–Meshkov flows under reshock conditions using large-eddy simulations. *J. Fluid Mech.* **670**, 439–480.
LOMBARDINI, M. & PULLIN, D.I. 2009 Startup process in the Richtmyer–Meshkov instability. *Phys. Fluids* **21**, 044104.
LUO, X., LIANG, Y., SI, T. & ZHAI, Z. 2019 Effects of non-periodic portions of interface on Richtmyer–Meshkov instability. *J. Fluid Mech.* **861**, 309–327.
MANSOOR, M.M., DALTON, S.M., MARTINEZ, A.A., DESJARDINS, T., CHARONKO, J.J. & PRESTRIDGE, K.P. 2020 The effect of initial conditions on mixing transition of the Richtmyer–Meshkov instability. *J. Fluid Mech.* **904**, A3.
MARIANI, C., VANDENBOOMGAERDE, M., JOURDAN, G., SOUFFLAND, D. & HOUAS, L. 2008 Investigation of the Richtmyer–Meshkov instability with stereolithographed interfaces. *Phys. Rev. Lett.* **100**, 254503.
MATSUOKA, C. & NISHIHARA, K. 2006*a* Analytical and numerical study on a vortex sheet in incompressible Richtmyer–Meshkov instability in cylindrical geometry. *Phys. Rev.* E **74**, 066303.
MATSUOKA, C. & NISHIHARA, K. 2006*b* Vortex core dynamics and singularity formations in incompressible Richtmyer–Meshkov instability. *Phys. Rev.* E **73**, 026304.
MESHKOV, E.E. 1969 Instability of the interface of two gases accelerated by a shock wave. *Fluid Dyn.* **4**, 101–104.
MIKAELIAN, K.O. 1994 Freeze-out and the effect of compressibility in the Richtmyer–Meshkov instability. *Phys. Fluids* **6**, 356–368.
MIKAELIAN, K.O. 2003 Explicit expressions for the evolution of single-mode Rayleigh–Taylor and Richtmyer–Meshkov instabilities at arbitrary Atwood numbers. *Phys. Rev.* E **67**, 026319.
MIKAELIAN, K.O. 2008 Limitations and failures of the Layzer model for hydrodynamic instabilities. *Phys. Rev.* E **78**, 015303.
NIEDERHAUS, C.E. & JACOBS, J.W. 2003 Experimental study of the Richtmyer–Meshkov instability of incompressible fluids. *J. Fluid Mech.* **485**, 243–277.
NISHIHARA, K., WOUCHUK, J.G., MATSUOKA, C., ISHIZAKI, R. & ZHAKHOVSKY, V.V. 2010 Richtmyer–Meshkov instability: theory of linear and nonlinear evolution. *Phil. Trans. R. Soc.* A **368**, 1769–1807.
NUCKOLLS, J., WOOD, L., THIESSEN, A. & ZIMMERMAN, G. 1972 Laser compression of matter to super-high densities: thermonuclear (CTR) applications. *Nature* **239**, 139–142.
QIAO, X. & LAN, K. 2021 Novel target designs to mitigate hydrodynamic instabilities growth in inertial confinement fusion. *Phys. Rev. Lett.* **126**, 185001.

RICHTMYER, R.D. 1960 Taylor instability in shock acceleration of compressible fluids. *Commun. Pure Appl. Maths* **13**, 297–319.

SADOT, O., EREZ, L., ALON, U., ORON, D., LEVIN, L.A., EREZ, G., BEN-DOR, G. & SHVARTS, D. 1998 Study of nonlinear evolution of single-mode and two-bubble interaction under Richtmyer–Meshkov instability. *Phys. Rev. Lett.* **80**, 1654–1657.

VANDENBOOMGAERDE, M., GAUTHIER, S. & MÜGLER, C. 2002 Nonlinear regime of a multimode Richtmyer–Meshkov instability: a simplified perturbation theory. *Phys. Fluids* **14**, 1111–1122.

VANDENBOOMGAERDE, M., SOUFFLAND, D., MARIANI, C., BIAMINO, L., JOURDAN, G. & HOUAS, L. 2014 An experimental and numerical investigation of the dependency on the initial conditions of the Richtmyer–Meshkov instability. *Phys. Fluids* **26**, 024109.

VELIKOVICH, A.L. & DIMONTE, G. 1996 Nonlinear perturbation theory of the incompressible Richtmyer–Meshkov instability. *Phys. Rev. Lett.* **76**, 3112–3115.

WANG, H., CAO, Q., CHEN, C., ZHAI, Z. & LUO, X. 2022 Experimental study on a light–heavy interface evolution induced by two successive shock waves. *J. Fluid Mech.* **953**, A15.

WOUCHUK, J.G. 2001 Growth rate of the linear Richtmyer–Meshkov instability when a shock is reflected. *Phys. Rev.* E **63**, 056303.

WOUCHUK, J.G. & NISHIHARA, K. 1996 Linear perturbation growth at a shocked interface. *Phys. Plasmas* **3**, 3761–3776.

WOUCHUK, J.G. & NISHIHARA, K. 1997 Asymptotic growth in the linear Richtmyer–Meshkov instability. *Phys. Plasmas* **4**, 1028–1038.

YANG, J., KUBOTA, T. & ZUKOSKI, E.E. 1993 Applications of shock-induced mixing to supersonic combustion. *AIAA J.* **31**, 854–862.

YANG, Y., ZHANG, Q. & SHARP, D.H. 1994 Small amplitude theory of Richtmyer–Meshkov instability. *Phys. Fluids* **6**, 1856–1873.

ZHANG, Q. & GUO, W. 2016 Universality of finger growth in two-dimensional Rayleigh–Taylor and Richtmyer–Meshkov instabilities with all density ratios. *J. Fluid Mech.* **786**, 47–61.

ZHANG, Q. & GUO, W. 2022 Quantitative theory for spikes and bubbles in the Richtmyer–Meshkov instability at arbitrary density ratios. *Phys. Rev. Fluids* **7**, 093904.

ZHANG, Q. & SOHN, S.I. 1997 Nonlinear theory of unstable fluid mixing driven by shock wave. *Phys. Fluids* **9**, 1106–1124.

ZHOU, Y. 2017*a* Rayleigh–Taylor and Richtmyer–Meshkov instability induced flow, turbulence, and mixing. I. *Phys. Rep.* **720–722**, 1–136.

ZHOU, Y. 2017*b* Rayleigh–Taylor and Richtmyer–Meshkov instability induced flow, turbulence, and mixing. II. *Phys. Rep.* **723–725**, 1–160.

ZHOU, Y., CLARK, T.T., CLARK, D.S., GLENDINNING, S.G., SKINNER, M.A., HUNTINGTON, C.M., HURRICANE, O.A., DIMITS, A.M. & REMINGTON, B.A. 2019 Turbulent mixing and transition criteria of flows induced by hydrodynamic instabilities. *Phys. Plasmas* **26**, 080901.

ZHOU, Y., *et al.* 2021 Rayleigh–Taylor and Richtmyer–Meshkov instabilities: a journey through scales. *Physica* D **423**, 132838.